Chapter 4

Description of the experiment

The measurements presented in this thesis were obtained using data taken by ALEPH at the Z peak during the years 1994-95. ALEPH was one of the four detectors[1] at the LEP accelerator (Large Electron Positron collider). In this chapter both LEP and the ALEPH detector are briefly described. For the latter, the performances relevant for the analyses are emphasized.

4.1 The LEP collider

The LEP collider [33, 34] was an e^+e^- storage ring with a 27 km circumference situated at the European Laboratory for Particle Physics (CERN) in Geneva, Switzerland. It was located in an underground tunnel (depth 80-137 m) spanning the French and Swiss territories, see Fig. 4.1. It was built to make precision studies of the Standard Model and to look for hints of new physics, and it was in operation from August 1989 till November 2000.

The beams were formed by bunches of electrons and positrons accelerated in opposite directions. They were steered to collide only in the 4 points where the detectors were placed.

The LEP injection chain started with a linear accelerator (LINAC) which accelerated electrons and positrons in two stages. In the first stage, the electrons were accelerated up to an energy of 200 MeV. Then, part of these electrons were used to produce positrons by collision with a tungsten target. In the second stage, both electrons and positrons were accelerated up to an energy of 600 MeV. The particles were then injected into a small

[1] the other three are DELPHI, L3 and OPAL

storage ring (the Electron Positron Accumulator, EPA) where they were separated into bunches and accumulated until the beam intensities achieved nominal values. Afterwards, the leptons were first injected into the Proton Synchrotron (PS) and then into the Super Proton Synchrotron (SPS) storage ring, where they were accelerated up to an energy of 20 GeV. Finally, the particles were injected into the LEP main ring and accelerated until they reached the collision energy.

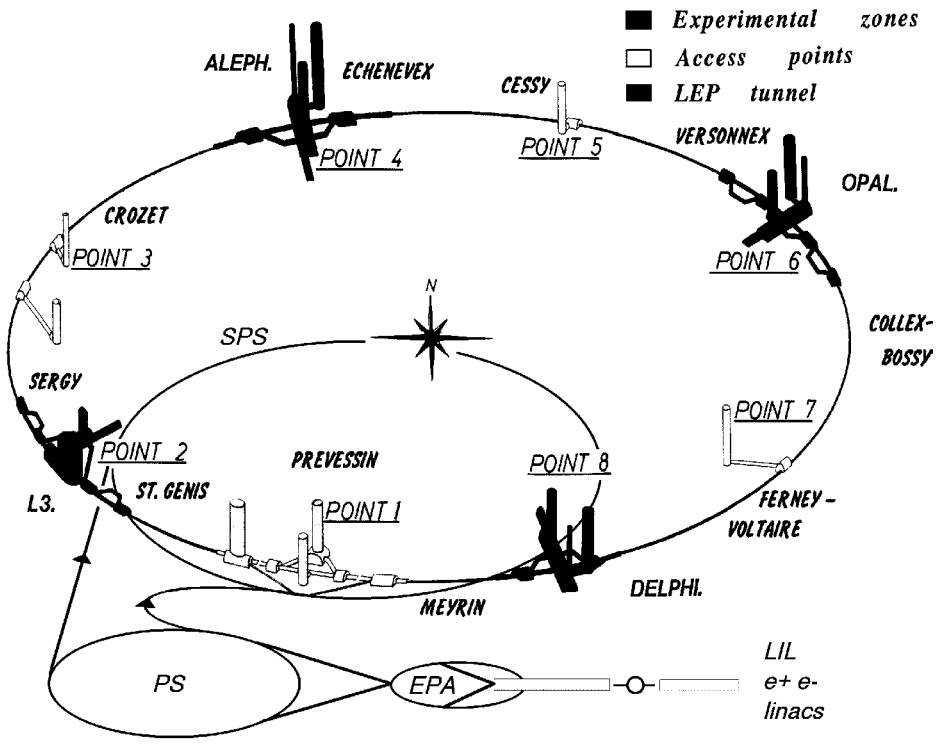

Figure 4.1: Schematic view of the LEP collider, the injector chain and the four interaction points.

During the first phase, LEP1 (1989-1995), LEP was operated at the peak position of the Z resonance and each experiment collected around four million visible Z decays. During the second phase, LEP2 (1995-2000), the energy was increased first to the threshold for W-pair production and later to the limit of the machine, which was found to be almost 210 GeV. Studies of the bosonic sector of the SM and searches for new physics have been the main goal of this last phase.

4.2 The ALEPH detector

The ALEPH (A detector for LEp PHysics) detector was a multi-purpose detector designed to cover as much of the 4π solid angle as possible. It consisted of a series of subdetectors arranged in an onion-like structure, see Fig. 4.2. A large tracking system immersed in a 1.5 T magnetic field allowed to reconstruct the direction and momentum of charged particles with very good resolution. The electromagnetic and hadronic calorimeters measured the energy of charged and neutral particles. The high segmentation of the first, together with the ionization measurement in the tracking system, was used for electron identification. Muons were identified using the muon chambers and the final planes of the hadron calorimeter, which provided continuous tracking inside sufficient iron absorber to eliminate the hadrons. The trigger system had the purpose of identifying interesting events while keeping the background rate low. Finally, the data acquisition system (DAQ) put together all the information coming from the subdetectors and built events which were then stored for further analysis.

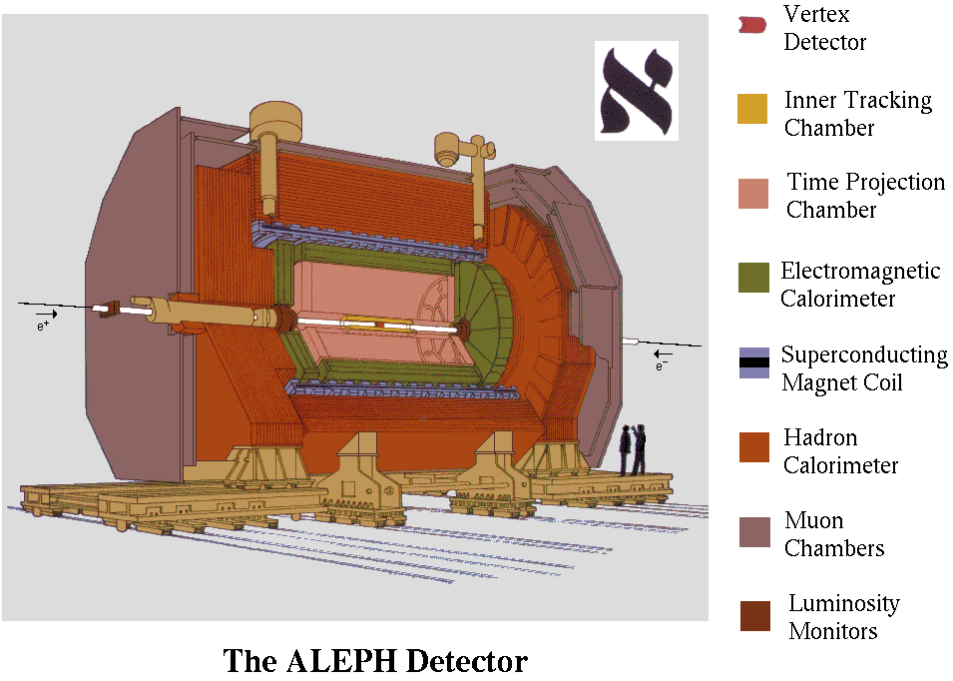

Figure 4.2: The ALEPH detector.

4.2.1 Subdetectors

In this section only the components relevant for this analysis are briefly described. We refer to [35] for further details.

- **Silicon Vertex detector (VDET):** The VDET was a double-sided silicon strip detector with two layers of strips parallel and perpendicular to the beam direction giving information on the azimuthal angle ϕ and the z coordinate, respectively. These were arranged in two coaxial cylinders around the beam pipe with inner and outer average radii of 6.5 and 11.3 cm. The angular acceptance was $|\cos\theta| \leq 0.95$ for tracks required to pass through at least one VDET layer.

  The trajectory of a track was determined starting with the outer tracking. VDET hits were used to improve the precision of the track parameters. They were reconstructed by averaging the charged-weighted positions of adjacent strips that have at least three times the mean noise charge. This way resolutions of $\sigma_\phi = 12$ μm in the ϕ and $\sigma_z = 10$ μm in the z direction were achieved. VDET also played a very important role in the identification of long-lived particles by tagging the displaced vertices of their decay products.

- **Inner Tracking Chamber (ITC):** It was a cylindrical multi-wire drift chamber. It provided up to eight accurate $r\phi$ points for tracking in the radial region between 16 and 26 cm. Charged particles traversing the chamber ionized the gas, which was a mixture of 80% Ar and 20% CO_2. The produced electrons drifted to the sense wires (mean drift velocity of 50 μm/ns), where they induced a signal via ionization avalanches. The ϕ coordinate was calculated from the relation between drift time and drift distance to the wire, whereas the z coordinate of a wire hit was found by using the difference of arrival times of the pulses at the two ends of the wire. The average accuracies were 150 μm and 3 cm, respectively.

- **Time Projection Chamber (TPC):** The central tracking device was a very large three-dimensional imaging drift chamber. It consisted of a cylindrical volume filled with a gas mixture of 91% Ar and 9% CH_4, and it operated with a gas pressure slightly above the atmospheric pressure. The electric drift field extended from each end plate towards the central membrane that divided the chamber into two halves. When a charged particle traversed the chamber, the electrons produced by ionization drifted towards one end plate, where their arrival position and time were measured by multi-wire proportional chambers. From the drift time and drift velocity the z coordinate could be deduced with a precision of 1 mm. The ϕ coordinate was calculated by interpolating the signals induced on cathode pads located behind

the sense wires, the r coordinate instead is given by the radial position of the pads involved in the measurement. There were 21 rows of cathode pads arranged in concentric circles around the axis. Thus, the TPC measured up to 21 three-dimensional space points per track.

Because of the magnetic field, the trajectory of a charged particle inside the TPC was a helix, and its projection onto the end plate was an arc of a circle. By measuring the curvature of such an arc, the transverse momentum (p_T) of tracks was determined. The TPC alone had a resolution of $\sigma(1/p_T) = 1.2 \times 10^{-3}(\mathrm{GeV/c})^{-1}$, measured with 45 GeV muons from Z decays. However, $\sigma(1/p_T) = 0.6 \times 10^{-3}(\mathrm{GeV/c})^{-1}$ could be achieved when the tracking information from VDET, ITC and TPC was combined.

In addition to its role as a tracking device, the TPC also contributed to the charged particle identification by measuring their energy loss by ionization per unit distance (dE/dx), as the size of the signal in the sense-wires (up to 340 for tracks traversing the full radial range) was proportional to this magnitude. Since dE/dx depends only on the particle velocity for a given material, a combination of dE/dx and momentum measurements allowed the mass, and thus the identity of the charged particle, to be deduced.

Figure 4.3 was extracted from the TPC online event display. It shows the view along the beam direction and the side view of a hadronic event in ALEPH.

- **Electromagnetic Calorimeter (ECAL):** It was a lead proportional wire chamber sampling calorimeter of a nominal thickness of 22 radiation lengths. It consisted of a barrel surrounding the TPC and was closed at each end by an end-cap. It lied inside the superconducting magnet coil to minimize the amount of material preceding it, and covered 98% of the solid angle. Photons, electrons and positrons interacted with the field of the lead atoms, thereby initiating electromagnetic showers through e^+e^- pair production and photon bremsstrahlung. The energy and position of each shower were read out using small cathode pads, which were connected internally to form towers which point to the interaction point and provided an average granularity of $0.9^\circ \times 0.9^\circ$. This fine segmentation provided excellent identification of photons, electrons and neutral pions within jets. The energy resolution for electromagnetic clusters was parameterized as $\sigma(E)/E = 0.18/\sqrt{E/\mathrm{GeV}} + 0.009$, and the angular resolution for photons $\sigma_{\theta,\phi} = (2.5/\sqrt{E/\mathrm{GeV}} + 0.25)\mathrm{mrad}$.

- **Hadronic Calorimeter (HCAL):** It was a sampling calorimeter consisting of layers of plastic streamer tubes separated by iron slabs. The iron structure was the main mechanical support of the ALEPH detector, and it served both as the return yoke of the magnet as well as a muon filter. HCAL was used to measure hadronic

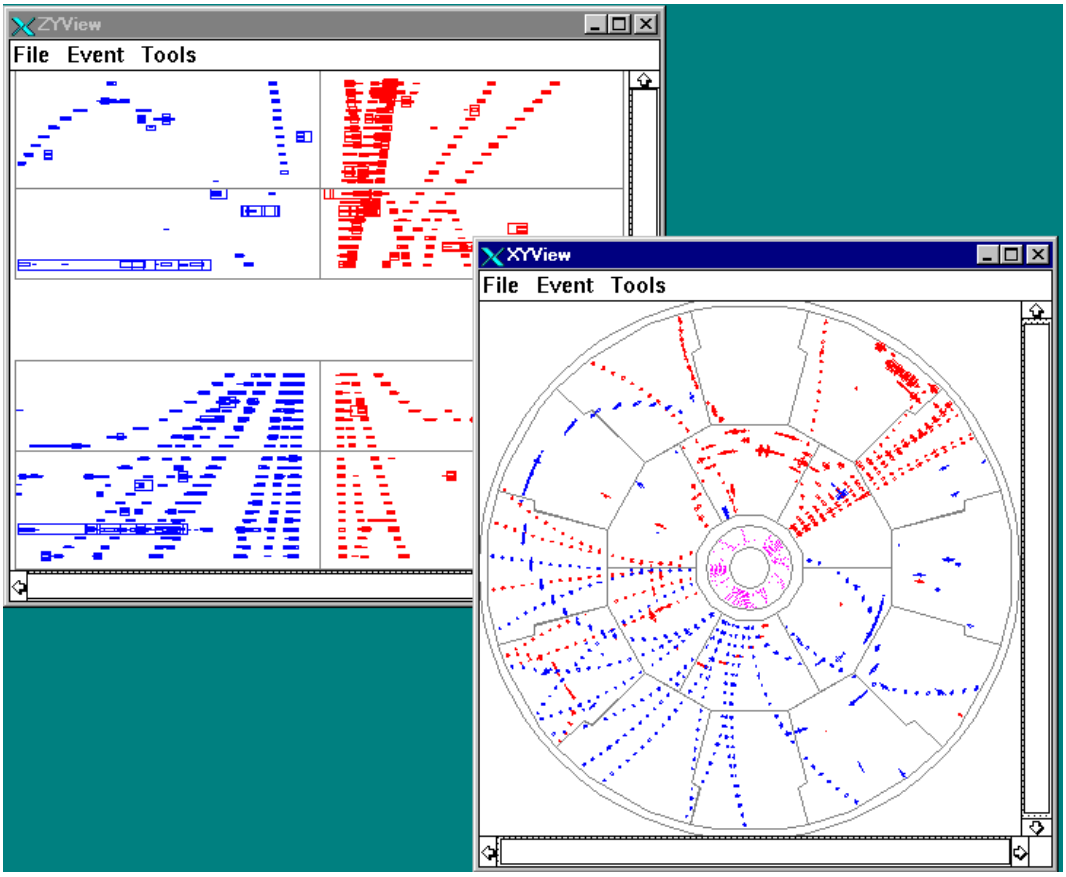

Figure 4.3: A hadronic event from the TPC online event display.

energy deposits (together with ECAL), and it was part of the muon identification system. It had a tower readout similar to ECAL with a granularity of $3.7° \times 3.7°$. In addition, a digital signal was recorded for each of the streamer tubes, providing a two-dimensional ($r\phi$) projection of the energy deposition. The energy resolution was $\sigma(E)/E = 0.85/\sqrt{E/\mathrm{GeV}}$.

- **Muon Chambers:** Muon identification was completed by the muon chambers, located beyond the HCAL. They were formed by two double layers of streamer tubes and gave a measurement of the x and y coordinates for tracks traversing the chambers.

4.2.2 The Trigger System

At LEP1 with four bunches per beam, a beam crossing occurred after every 22 μsec. If we take into account the LEP luminosity and the hadronic cross section, one hadronic

Z decay was expected every 0.3 sec on average. The purpose of the trigger system was to identify events coming from electron-positron annihilation while reducing the rate of background events. The main background came from collisions of beam particles with residual gas in the beam pipe, bremsstrahlung photons, off-momentum beam electrons which hit the beam pipe walls, and cosmic rays traversing the detector top to bottom. As every time an event was recorded by ALEPH, the information from all the subdetectors had to be read out, collected and combined to make a complete picture of the event, the trigger system also had to filter the events in order not to exceed the storage capacity, to minimize the dead time due to the detector read out, and to reduce the time that the TPC gate was open.

The requirements of the system lead to a three-level system. Level-1 decided within 5 μsec after the beam crossing whether or not to read out all detector elements. It had to identify whether there was a good charged track (from the ITC) and/or particle energy (from the calorimeters) to justify waiting for the TPC trigger signals. An important task of the Level-1 trigger was to keep the TPC operational, by deciding when the gate should be kept open for the full drift time. The Level-2 trigger simply seeked to verify a Level-1 charged track trigger by replacing the ITC tracking information with that from the TPC. It occurred about 50 μsec after beam crossing. A Level-3 software trigger was used to reduce the amount of recorded data by eliminating unwanted events.

Hadronic Z decays were collected using a Level-1 trigger in which energy deposits in ECAL were greater than 6 GeV in the barrel or 3 GeV in the end-cap or greater than 1.5 GeV in both end-caps in coincidence. A second Level-1 trigger possibility was that track segments in the drift chamber coincided with hits in a module of the hadron calorimeter, so requiring a certain penetration depth. This trigger was sensitive to muons and, with lower efficiency, to hadrons. The combination of these trigger requirements provided an efficiency of greater than 99.9% for selecting hadronic decays.

4.2.3 Data Acquisition System

Following a Level-2 YES decision, the data acquisition system (DAQ) was in charge of handling the information from all the subdetectors. The ALEPH DAQ was organized in a tree structure, with a strong hierarchy, implying that components on the same level do not communicate with each other. The different subdetectors readout was performed in parallel and asynchronously. The information was collected in a microprocessor called the Main Event Builder, where it was synchronized. The date was then sent to a computer

in the surface where it was checked by the Level-3 software and finally written to disk.

4.2.4 Energy Flow Determination

The Energy Flow algorithm [36] was meant to improve the visible energy resolution in ALEPH by combining the measurements of track momenta, calorimeter energy deposits and particle identification. It built a set of *energy flow objects* (electrons, muons, photons, charged and neutral hadrons) which should be a close representation of the stable particles actually produced in the collision.

In a first stage, charged tracks and calorimeter clusters were subjected to a cleaning procedure to reject badly reconstructed tracks and noise from the calorimeters. Then the charged particle tracks were extrapolated to the calorimeters, and groups of topologically connected tracks and clusters (called *calorimeter objects*) were formed. From these calorimeter objects the following pieces were then removed:

- Charged tracks identified as electrons, together with the associated energy in ECAL. If the energy in the calorimeter was larger than expected within a certain range, the excess energy was assumed to come from a bremsstrahlung photon, and it was counted as neutral electromagnetic energy.
- Charged tracks identified as muons, together with a maximum of 1 GeV from the closest associated ECAL deposit (if any) and a maximum of 400 MeV per plane fired around the extrapolation of the muon track from the corresponding HCAL cluster.
- identified photons and π^0s (they are counted as neutral electromagnetic energy).

At this point only charged and neutral hadrons should be left in the calorimeters. Charged hadrons were identified as all the remaining charged tracks, and the pion mass was assumed for them. Neutral hadrons were identified as a significant excess of calorimeter energy.

Using the energy flow algorithm, the resulting energy resolution was parameterized as

$$\frac{\sigma(E)}{E} = \frac{(0.59 \pm 0.03)}{\sqrt{E/\mathrm{GeV}}} + (0.6 \pm 0.3),$$

which represents a factor of two improvement with respect to the energy resolution obtained when adding up the raw energy of the calorimetric cells.

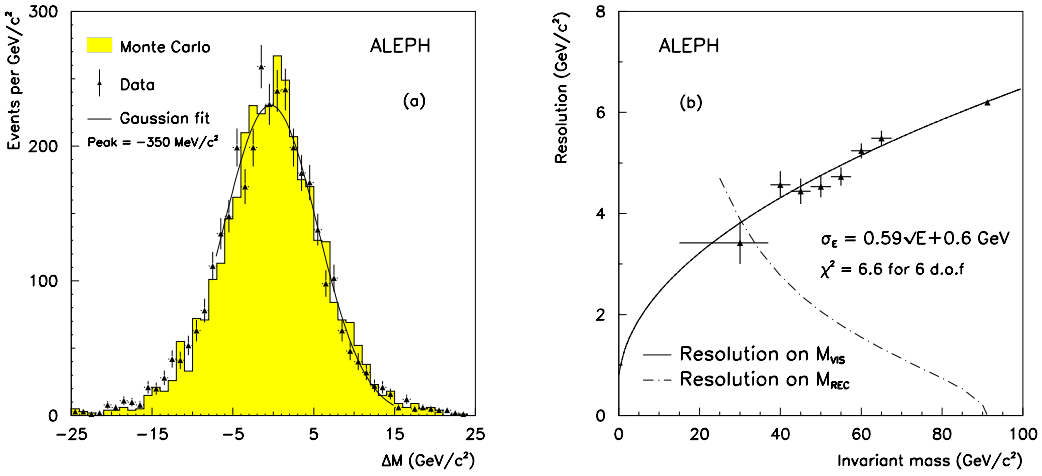

Figure 4.4: (a) Distribution of Δm for hadronic events accompanied by an isolated-energetic photon, both for Data and Monte Carlo. (b) Evolution of the resolution on $m_{\rm vis}$ and $m_{\rm rec}$ with the hadronic mass. The full line indicates the result of the fit to a calorimetric-like resolution.

The estimation of the energy resolution was done with 3225 ALEPH hadronic events accompanied by an isolated energetic photon (or π^0). For each event, the invariant mass of the system is calculated by two methods: the direct determination of the visible mass, $m_{\rm vis}$, using the energy flow algorithm, and the computation of the mass $m_{\rm rec}$ recoiling against the well-determined photon energy. Then, the distribution $\Delta m = m_{\rm vis} - m_{\rm rec}$ was measured and showed a good agreement with the one coming from fully simulated hadronic events, see Fig. 4.4 (a). However, since the resolution achieved for $m_{\rm rec}$ depends strongly on the hadronic mass, the event sample had to be divided into several subsamples to compute the corresponding resolution on $m_{\rm vis}$; this was calculated by unfolding the contribution from $m_{\rm rec}$ from the resolution on Δm. Fig. 4.4(b) shows the result of the fit.

Chapter 5

Analysis Description

Lo que sabe hacer no lo enseñan en la escuela,
que es materia superior.
Pudo ser mejor, pero nuestro baile acaba.

Two kinds of measurements have been performed in the present thesis. First, measurements of the strong coupling constant from the four-jet rate were performed. Second, a simultaneous measurement of the strong coupling constant and the colour factors was performed using the four-jet rate and the four-jet angular correlations, all of them as defined in Chapter 3. The results of these analyses will be discussed in the next chapter. Here, the analysis procedure, common to both measurements, is described.

First, some details of the event selection are given. Then, the theoretical predictions are described, followed by an explanation of the corrections applied to have a theoretical prediction at detector level to be compared to the data. Afterwards, the strategy of the fit procedure is given. Finally, the sources of systematic uncertainty studied as well as the method used to combine the different contributions into the total systematic error are detailed.

5.1 Event Selection

Y quedaba mucho por hacer.
Limpiar de malas hierbas el prado,
arrancar las rejas y cercados.

In the analyses data from 1994 and 1995 are used, taken at and around the Z peak by the ALEPH detector. First a hadronic selection is applied. Charged particle tracks

are selected that have at least four measured space coordinates from the TPC, a polar angle in the range $18^\circ < \theta < 162^\circ$, and a transverse momentum with respect to the beam direction of $p_t > 0.2$ GeV/c. In addition, the closest radial distance of approach of the extrapolated track to the beam axis, d_0, is required to be less than 2 cm, and the z coordinate of the point of closest radial approach, z_0, is required to be less than 10 cm. Using these selected charged tracks, the total charged energy $E_{\rm ch} = \sum_i \sqrt{p_i^2 + m_\pi^2}$ is computed. A minimum of four tracks are requested for the TPC as studies on the track finding efficiency showed that in hadronic Z events 98.6% of tracks that cross at least four pad rows in the TPC are successfully reconstructed [37].

Neutral energy-flow objects are kept if their polar angle with respect to the beam axis is in the range $18^\circ < \theta < 162^\circ$. This cut is applied in order to avoid the low angle regions since for neutral particles these regions are not well described by the detector simulation. Events are selected that have at least five selected charged particle tracks and $E_{\rm ch} > 15$ GeV. Only events with $|\cos\Theta_{\rm Sph}| < 0.9$ are kept, where $\Theta_{\rm Sph}$ is the polar angle of the sphericity axis, computed from all charged and neutral particles as obtained from the energy-flow algorithm.

The sphericity axis is defined as follows. The momentum tensor $M_{\alpha\beta} = \sum_j p_{\alpha j} p_{\beta j}$, can be diagonalized so that its normalized eigenvalues Q_i fulfill $Q_1 + Q_2 + Q_3 = 1$. If they are ordered such that $0 < Q_1 < Q_2 < Q_3$, then the Sphericity is defined as $S = \frac{3}{2}(Q_1 + Q_2)$. The eigenvector $\vec{n}_3$ determines the sphericity axis, and $\vec{n}_2$ and $\vec{n}_3$ define the event plane. The cut on the sphericity axis ensures that the event is well contained within the detector.

According to the MC simulation, this basic hadronic event selection is about 90.2% efficient. Non-hadronic background, which is dominated by $\tau^+\tau^-$ events, represents about 0.3% of this sample. After the selection, a sample of 2.5 million hadronic events remains for further analysis.

The hadronic events are clustered into four jets by means of the Durham clustering algorithm [38], with the E recombination scheme. The metric

$$y_{ij} = \frac{2\min(E_i^2, E_j^2)}{E_{\rm vis}^2}(1 - \cos\theta_{ij}) \tag{5.1}$$

is used, i.e. those particles (i and j) with the smallest y_{ij} are clustered together to form a new pseudo-particle with four-momentum

$$E_{\rm new} = E_i + E_j \quad , \quad \vec{p}_{\rm new} = \vec{p}_i + \vec{p}_j \, . \tag{5.2}$$

The clustering procedure is repeated until four jets are left. Finally, the event is further used provided that the fraction of electromagnetic energy in each jet is smaller than 90%, to avoid high energy photons coming from final state radiation from quarks. At this point, all the selected events are used for the calculation of the four-jet rate, when the number of four-jet events at each resolution parameter value is obtained.

Next, the energies of the jets are subsequently rescaled, to improve the resolution, by imposing total energy-momentum conservation. The assumption that the four jet directions are perfectly measured is made, since ALEPH has better angular than energy resolution. Thus, the following system of linear equations is solved in order to find the rescaled energies E_i, which are required to be positive:

$$\begin{aligned} \vec{\beta}_1 E_1 + \vec{\beta}_2 E_2 + \vec{\beta}_3 E_3 + \vec{\beta}_4 E_4 &= \vec{0} \\ E_1 + E_2 + E_3 + E_4 &= \sqrt{s} \end{aligned} \tag{5.3}$$

The velocities $\vec{\beta}_i = \vec{p}_i^{\,\mathrm{meas}}/E_i^{\mathrm{meas}}$ are fixed, $\vec{p}_i^{\,\mathrm{meas}}$ and E_i^{meas} are the measured momentum and energy. The Durham metric is recalculated and the event is taken as a four-jet event if $\min_{ij=1,4} y_{ij} > y_{\mathrm{cut}}$, with $\mathrm{y_{cut}}$=0.008. For this resolution parameter, $\mathrm{y_{cut}}$, the number of events selected for the calculation of the four-jet angular correlations is about 163,000. The chosen $\mathrm{y_{cut}}$ value represents a compromise between high statistics and good separation of the four jets.

The binned distributions of the angular correlations and the four-jet rate for different values of the resolution parameter are computed taking all selected charged and neutral energy-flow objects. Twenty equally-sized bins are used for each angular observable, and the four-jet rate is measured at 60 equidistant points in the range $-12 \leq \ln(\mathrm{y_{cut}}) \leq -0.2$.

The analyses also use 5.3 million simulated hadronic events produced with a generator based on the JETSET 7.4 parton shower model. The production rates, decay modes and lifetimes of heavy hadrons are adjusted to agree with recent measurements, while heavy quarks are fragmented using the Peterson *et al.* model [39]. Detector effects are simulated using the GEANT package [40].

5.2 The Theoretical Prediction

The NLO perturbative predictions for the angular correlations and the four-jet rate were obtained with the MC program DEBRECEN 2.0 [41].

DEBRECEN is a collection of C++ libraries that implement the dipole formalism for calculating next-to-leading order corrections to multi-jet final states. The version used in the analyses of this thesis contains programs that can be used to calculate the gauge group independent kinematical functions, see Eqs. 3.7 and 3.8, at leading and next-to-leading order for any three- and four-jet-like quantity as well as the leading order functions for the production of five jets in electron-positron annihilation. These functions can be calculated either in the pure QCD case, or taking into account the contributions from a light gluino. This second option will be referred to as the QCD+gluino case. Only infrared- and collinear-safe observables can be calculated with DEBRECEN. These quantities have to be experimentally (theoretically) defined in such a way that their actual value is independent of the number of soft and collinear hadrons (partons) produced in the final state.

More than 100 million events were generated using DEBRECEN. The coefficients of the B and C functions can be found in Tables 5.1, 5.2, 5.3, 5.4, 5.5, 5.6, 5.7, 5.8 for the four-jet angular correlations, and in Tables 5.9, 5.10 and 5.11 for the four-jet rate, where the third table gives the added functions when taking $SU(3)$ values for the colour factor ratios. These combined functions are the ones to be used for the measurement of the strong coupling constant from the four-jet rate.

5.3 Corrections

5.3.1 Hadronization Corrections

The theoretical predictions have to be corrected to take into account hadronization as well as detector effects before being compared to data. The hadronization corrections have been implemented separately for the four-jet rate and the angular correlations as detailed below.

Corrections for R_4

For the four-jet rate, for which the resummation of large logarithms exists, the hadronization corrections have been computed using R_4 distributions at parton and at hadron level. Here, the parton level refers to the set of partons present after the showering process. Then the correction factors for each y_{cut} are computed according to

$$C^{had}(y_{cut}) = \frac{R_4^{had}(y_{cut})}{R_4^{part}(y_{cut})} \quad . \tag{5.4}$$

$\lvert\cos\chi_{\rm BZ}\rvert$	$B_0(y_{\rm cut})$	$B_x(y_{\rm cut})$	$B_y(y_{\rm cut})$
0.025	37.68 ± 0.06	1.96 ± 0.01	11.99 ± 0.01
0.075	37.70 ± 0.06	1.91 ± 0.01	11.85 ± 0.01
0.125	37.30 ± 0.06	2.05 ± 0.01	11.68 ± 0.01
0.175	37.42 ± 0.06	2.14 ± 0.01	11.50 ± 0.01
0.225	37.17 ± 0.06	2.22 ± 0.01	11.28 ± 0.01
0.275	37.54 ± 0.05	2.38 ± 0.01	10.98 ± 0.01
0.325	38.18 ± 0.06	2.44 ± 0.01	10.75 ± 0.01
0.375	38.54 ± 0.05	2.712 ± 0.009	10.48 ± 0.01
0.425	39.58 ± 0.06	2.795 ± 0.009	10.17 ± 0.01
0.475	40.27 ± 0.05	3.049 ± 0.009	9.86 ± 0.01
0.525	41.51 ± 0.06	3.227 ± 0.009	9.49 ± 0.01
0.575	43.08 ± 0.06	3.48 ± 0.01	9.175 ± 0.009
0.625	44.59 ± 0.05	3.79 ± 0.01	8.844 ± 0.008
0.675	47.36 ± 0.06	4.13 ± 0.01	8.556 ± 0.007
0.725	50.21 ± 0.06	4.51 ± 0.01	8.230 ± 0.007
0.775	54.08 ± 0.06	4.98 ± 0.01	7.934 ± 0.006
0.825	58.47 ± 0.06	5.46 ± 0.01	7.648 ± 0.006
0.875	64.43 ± 0.06	6.18 ± 0.01	7.383 ± 0.005
0.925	73.74 ± 0.07	7.57 ± 0.02	7.655 ± 0.005
0.975	155.1 ± 0.1	17.20 ± 0.02	13.933 ± 0.006

Table 5.1: B functions at different values of $\lvert\cos\chi_{\rm BZ}\rvert$ from DEBRECEN. The first column shows the center of bin value.

The superscript "had" ("part") refers to the hadron (parton) level. The prediction corrected to hadron level (HL), $R_4^{\rm corrHL}(y_{\rm cut})$, is obtained from the theoretical prediction, $R_4^{\rm TH}(y_{\rm cut})$, according to

$$R_4^{\rm corrHL}(y_{\rm cut}) = C^{\rm had}(y_{\rm cut}) R_4^{\rm TH}(y_{\rm cut}) \quad . \tag{5.5}$$

The JETSET parton shower model together with the Lund string fragmentation scheme (PYTHIA 6.1) is employed for the calculation of the hadronization corrections. The model parameters have been taken from [37], with the exception that final state radiation is not included in the simulation.

A similar approach for the description of the parton level is taken by the HERWIG

$\lvert\cos\chi_{\rm BZ}\rvert$	$C_0(y_{\rm cut})$	$C_x(y_{\rm cut})$	$C_y(y_{\rm cut})$	$C_{xx}(y_{\rm cut})$	$C_{xy}(y_{\rm cut})$	$C_{yy}(y_{\rm cut})$
0.025	-174 ± 7	762 ± 13	-1653 ± 7	26 ± 4	161 ± 3	-400.9 ± 0.6
0.075	-166 ± 10	715 ± 18	-1647 ± 9	36 ± 5	144 ± 15	-396.0 ± 0.6
0.125	-177 ± 10	745 ± 18	-1653 ± 9	30 ± 5	162 ± 15	-389.8 ± 0.6
0.175	-171 ± 13	726 ± 17	-1633 ± 8	38 ± 5	140 ± 4	-382.0 ± 0.5
0.225	-157 ± 12	751 ± 32	-1646 ± 7	27 ± 8	135 ± 5	-373.6 ± 0.5
0.275	-171 ± 11	748 ± 33	-1659 ± 8	45 ± 8	126 ± 4	-364.5 ± 0.5
0.325	-149 ± 13	727 ± 18	-1678 ± 8	43 ± 5	111 ± 3	-354.9 ± 0.5
0.375	-177 ± 11	753 ± 17	-1691 ± 8	44 ± 5	94 ± 4	-343.9 ± 0.5
0.425	-172 ± 8	787 ± 17	-1720 ± 8	51 ± 5	81 ± 3	-333.9 ± 0.4
0.475	-179 ± 22	830 ± 26	-1771 ± 7	41 ± 7	66 ± 3	-324.6 ± 0.4
0.525	-180 ± 25	789 ± 29	-1817 ± 7	63 ± 8	49 ± 3	-313.1 ± 0.4
0.575	-161 ± 18	831 ± 21	-1874 ± 7	70 ± 6	25 ± 3	-301.9 ± 0.4
0.625	-186 ± 9	906 ± 18	-1973 ± 7	68 ± 4	3 ± 2	-291.3 ± 0.3
0.675	-191 ± 10	913 ± 15	-2066 ± 6	80 ± 4	-19 ± 2	-281.3 ± 0.3
0.725	-222 ± 11	1011 ± 13	-2196 ± 6	80 ± 4	-44 ± 2	-271.1 ± 0.3
0.775	-242 ± 9	1088 ± 13	-2354 ± 6	83 ± 3	-74 ± 2	-261.0 ± 0.3
0.825	-276 ± 10	1179 ± 16	-2567 ± 6	105 ± 4	-111 ± 2	-252.0 ± 0.2
0.875	-287 ± 12	1277 ± 20	-2827 ± 6	123 ± 5	-151 ± 2	-243.6 ± 0.2
0.925	-346 ± 12	1511 ± 20	-3256 ± 7	144 ± 4	-214 ± 2	-248.8 ± 0.2
0.975	-752 ± 12	3129 ± 16	-6849 ± 9	320 ± 5	-562 ± 3	-444.3 ± 0.2

Table 5.2: C functions at different values of $\lvert\cos\chi_{\rm BZ}\rvert$ from DEBRECEN. $C_z(y_{\rm cut})$ was found to be very small and therefore is not tabulated. The first column shows the center-of-bin value.

6.1 program. However, there the fragmentation is modelled according to the cluster fragmentation scheme.

Two similar and extreme approaches can be tested by using the matrix element (ME) option in the PYTHIA program, or a special PYTHIA production which has on average four partons after the parton shower. In order to achieve this the parton shower cut-off parameter, Q_0, has been increased to 4 GeV, and afterwards the fragmentation parameters have been retuned so that the hadron level describes the data (this approach will be called PYTHIA,Q_0 from now on). In the ME option (namely PYTHIA,ME) at the parton level two-, three- and four-parton final states are generated according to the exact NLO matrix elements, and then the hadronization step is performed via the string fragmentation scheme. This model should give a better description of four-jet related quantities.

$\cos\Phi_{\mathrm{KSW}}$	$B_0(\mathrm{y_{cut}})$	$B_x(\mathrm{y_{cut}})$	$B_y(\mathrm{y_{cut}})$
-0.95	34.66 ± 0.03	6.39 ± 0.01	3.917 ± 0.002
-0.85	20.22 ± 0.02	3.725 ± 0.007	3.602 ± 0.003
-0.75	19.25 ± 0.02	3.627 ± 0.007	4.569 ± 0.004
-0.65	18.97 ± 0.02	3.543 ± 0.007	5.214 ± 0.005
-0.55	19.49 ± 0.02	3.435 ± 0.006	5.682 ± 0.006
-0.45	20.03 ± 0.02	3.208 ± 0.005	5.934 ± 0.006
-0.35	20.90 ± 0.02	2.985 ± 0.005	6.062 ± 0.007
-0.25	21.87 ± 0.03	2.746 ± 0.004	6.132 ± 0.007
-0.15	22.62 ± 0.03	2.460 ± 0.003	6.011 ± 0.007
-0.05	23.62 ± 0.03	2.222 ± 0.003	5.767 ± 0.007
0.05	21.41 ± 0.03	1.689 ± 0.003	5.242 ± 0.006
0.15	20.76 ± 0.03	1.417 ± 0.003	4.838 ± 0.005
0.25	20.69 ± 0.03	1.186 ± 0.003	4.539 ± 0.005
0.35	20.98 ± 0.03	0.941 ± 0.003	4.261 ± 0.005
0.45	21.33 ± 0.03	0.764 ± 0.004	4.046 ± 0.004
0.55	22.32 ± 0.03	0.630 ± 0.005	3.873 ± 0.004
0.65	23.81 ± 0.03	0.487 ± 0.005	3.798 ± 0.004
0.75	26.63 ± 0.03	0.381 ± 0.006	3.828 ± 0.004
0.85	32.90 ± 0.04	0.211 ± 0.007	4.197 ± 0.004
0.95	74.52 ± 0.06	0.05 ± 0.01	8.185 ± 0.005

Table 5.3: B functions at different values of $\cos\Phi_{\mathrm{KSW}}$ from DEBRECEN. The first column shows the center-of-bin value.

However, it is known not to describe well the energy evolution of basic quantities such as the charged multiplicity [42].

Corrections for the angular observables

For the angular correlations a different MC simulation is used. Still using PYTHIA 6.1, the option to start a parton shower from a four-parton configuration is chosen [43]. This MC simulation should better describe our data provided that two- and three-jet backgrounds are negligible, and that the showering and hadronization processes are well modelled. The parameters for the showering and hadronization are identical to the simulation used for the four-jet rate.

$\cos\Phi_{\rm KSW}$	$C_0(y_{\rm cut})$	$C_x(y_{\rm cut})$	$C_y(y_{\rm cut})$	$C_{xx}(y_{\rm cut})$	$C_{xy}(y_{\rm cut})$	$C_{yy}(y_{\rm cut})$
-0.95	-158 ± 3	653 ± 4	-1501 ± 2	129 ± 2	-236 ± 1	-128.06 ± 0.09
-0.85	-81 ± 3	378 ± 5	-884 ± 3	77 ± 1	-112 ± 1	-125.0 ± 0.1
-0.75	-73 ± 3	355 ± 4	-832 ± 3	74 ± 2	-88 ± 1	-158.8 ± 0.2
-0.65	-72 ± 3	350 ± 4	-829 ± 3	74 ± 2	-66 ± 2	-180.6 ± 0.2
-0.55	-75 ± 3	367 ± 6	-848 ± 3	71 ± 2	-47 ± 1	-194.9 ± 0.2
-0.45	-83 ± 5	377 ± 7	-878 ± 3	63 ± 2	-31 ± 2	-203.4 ± 0.3
-0.35	-76 ± 5	394 ± 7	-908 ± 5	60 ± 2	-17 ± 2	-206.3 ± 0.3
-0.25	-93 ± 3	427 ± 6	-957 ± 4	51 ± 1	2 ± 2	-205.3 ± 0.3
-0.15	-92 ± 3	429 ± 6	-995 ± 4	49 ± 1	8 ± 1	-201.0 ± 0.3
-0.05	-106 ± 7	464 ± 5	-1035 ± 4	42 ± 1	16 ± 1	-192.0 ± 0.3
0.05	-81 ± 7	430 ± 7	-953 ± 4	30 ± 1	32 ± 1	-174.1 ± 0.2
0.15	-95 ± 4	420 ± 6	-915 ± 4	23 ± 1	37 ± 1	-158.7 ± 0.2
0.25	-88 ± 4	415 ± 5	-910 ± 4	20 ± 1	42 ± 1	-147.3 ± 0.2
0.35	-86 ± 4	424 ± 5	-915 ± 3	16 ± 1	44 ± 1	-137.2 ± 0.2
0.45	-102 ± 4	445 ± 5	-937 ± 3	8 ± 1	49.8 ± 0.9	-129.1 ± 0.2
0.55	-103 ± 4	450 ± 5	-971 ± 3	8 ± 1	50.6 ± 0.9	-123.1 ± 0.2
0.65	-113 ± 4	496 ± 6	-1049 ± 3	2 ± 1	56.2 ± 0.9	-119.5 ± 0.1
0.75	-128 ± 5	549 ± 7	-1178 ± 3	0 ± 2	65 ± 2	-120.2 ± 0.1
0.85	-163 ± 7	684 ± 7	-1448 ± 3	-7 ± 2	78 ± 1	-130.6 ± 0.1
0.95	-398 ± 6	1581 ± 8	-3320 ± 5	-33 ± 3	176 ± 2	-251.3 ± 0.2

Table 5.4: C functions at different values of $\cos\Phi_{\rm KSW}$ from DEBRECEN. $C_z(y_{\rm cut})$ was found to be very small and therefore is not tabulated. The first column shows the center-of-bin value.

An important parameter in this four-parton MC simulation is the so called intrinsic jet resolution parameter $y_{\rm int}$. The rejection of four-parton configurations with a y_{34} (jet resolution parameter when going from four to three jets) smaller than $y_{\rm int}$ is used to avoid soft and collinear divergences. The parameter $y_{\rm int}$ has to be smaller than $y_{\rm cut}$, but going to very small values is not possible for technical reasons. Therefore, it is not a suitable MC for the four-jet rate, which is calculated at different $y_{\rm cut}$ values over a large range. The value used for the MC simulation in order to correct the angular distributions was $y_{\rm int}$=0.004.

Using this four-parton option 15 million events were generated with about 8 million four-jet events selected at $y_{\rm cut} = 0.008$. The angular distributions are calculated at three levels: parton level before showering (i.e. using massless LO matrix elements for 4 par-

$\lvert\cos\theta_{\rm NR}\rvert$	$B_0(\mathrm{y_{cut}})$	$B_x(\mathrm{y_{cut}})$	$B_y(\mathrm{y_{cut}})$
0.025	39.96 ± 0.05	2.76 ± 0.01	13.72 ± 0.01
0.075	40.49 ± 0.05	2.80 ± 0.01	13.65 ± 0.01
0.125	40.29 ± 0.05	2.92 ± 0.01	13.53 ± 0.01
0.175	41.03 ± 0.05	2.91 ± 0.01	13.33 ± 0.01
0.225	41.38 ± 0.05	3.04 ± 0.01	13.13 ± 0.01
0.275	42.42 ± 0.05	3.23 ± 0.01	12.74 ± 0.01
0.325	42.97 ± 0.05	3.32 ± 0.01	12.30 ± 0.01
0.375	44.56 ± 0.05	3.43 ± 0.01	11.94 ± 0.01
0.425	45.77 ± 0.06	3.64 ± 0.01	11.42 ± 0.01
0.475	47.40 ± 0.06	3.91 ± 0.01	10.89 ± 0.01
0.525	49.02 ± 0.06	4.12 ± 0.01	10.32 ± 0.01
0.575	50.96 ± 0.06	4.37 ± 0.01	9.682 ± 0.009
0.625	52.93 ± 0.06	4.63 ± 0.01	9.052 ± 0.009
0.675	55.38 ± 0.06	4.83 ± 0.01	8.396 ± 0.008
0.725	57.52 ± 0.07	5.08 ± 0.01	7.654 ± 0.007
0.775	59.59 ± 0.07	5.32 ± 0.01	6.930 ± 0.006
0.825	60.97 ± 0.07	5.52 ± 0.01	6.155 ± 0.005
0.875	61.31 ± 0.07	5.73 ± 0.01	5.411 ± 0.004
0.925	63.00 ± 0.07	6.00 ± 0.01	4.773 ± 0.004
0.975	77.03 ± 0.08	6.64 ± 0.02	4.371 ± 0.003

Table 5.5: B functions at different values of $|\cos\theta_{\rm NR}|$ from DEBRECEN. The first column shows the center-of-bin value.

tons), parton level after showering and hadron level. In order to correct not only for the hadronization effects, but also for the missing higher orders, the bin-by-bin ratios of the distribution at hadron level over the one at parton level are calculated,

$$C^{\rm bck+had}(i_{bin}) = \frac{\cos X^{\rm had}(i_{bin})}{\cos X^{\rm part}(i_{bin})} \quad , \tag{5.6}$$

where now "part" refers to parton level before showering. The predictions corrected to hadron level are then obtained as

$$\cos X^{\rm corrHL}(i_{bin}) = C^{\rm bck+had}(i_{bin}) \cos X^{\rm TH}(i_{bin}) \quad . \tag{5.7}$$

$\lvert\cos\theta_{\rm NR}\rvert$	$C_0(y_{\rm cut})$	$C_x(y_{\rm cut})$	$C_y(y_{\rm cut})$	$C_{xx}(y_{\rm cut})$	$C_{xy}(y_{\rm cut})$	$C_{yy}(y_{\rm cut})$
0.025	-175 ± 5	746 ± 8	-1760 ± 7	46 ± 3	156 ± 3	-453.1 ± 0.6
0.075	-174 ± 14	749 ± 14	-1770 ± 9	52 ± 6	134 ± 16	-452.2 ± 0.6
0.125	-162 ± 14	786 ± 14	-1771 ± 10	41 ± 6	161 ± 16	-450.1 ± 0.6
0.175	-174 ± 6	768 ± 10	-1773 ± 12	53 ± 4	140 ± 5	-438.6 ± 0.6
0.225	-159 ± 6	785 ± 10	-1815 ± 11	52 ± 4	135 ± 5	-434.2 ± 0.6
0.275	-171 ± 7	791 ± 11	-1851 ± 8	54 ± 4	108 ± 5	-418.7 ± 0.5
0.325	-183 ± 6	832 ± 22	-1892 ± 9	58 ± 7	102 ± 4	-409.6 ± 0.5
0.375	-191 ± 6	839 ± 22	-1938 ± 9	59 ± 6	84 ± 4	-394.1 ± 0.5
0.425	-183 ± 7	888 ± 11	-1991 ± 8	65 ± 4	71 ± 3	-379.6 ± 0.4
0.475	-209 ± 7	932 ± 12	-2078 ± 8	68 ± 4	47 ± 3	-360.9 ± 0.4
0.525	-218 ± 7	963 ± 12	-2141 ± 7	72 ± 3	21 ± 3	-342.1 ± 0.4
0.575	-224 ± 7	1021 ± 13	-2237 ± 8	76 ± 3	-6 ± 3	-322.2 ± 0.4
0.625	-237 ± 7	1058 ± 13	-2330 ± 9	89 ± 6	-27 ± 3	-298.5 ± 0.3
0.675	-262 ± 8	1113 ± 13	-2438 ± 8	82 ± 5	-55 ± 3	-275.8 ± 0.3
0.725	-258 ± 8	1188 ± 11	-2530 ± 7	92 ± 4	-84 ± 4	-251.8 ± 0.3
0.775	-274 ± 11	1228 ± 15	-2616 ± 8	101 ± 4	-112 ± 2	-226.2 ± 0.2
0.825	-277 ± 14	$1265. \pm 14.$	-2677 ± 7	101 ± 4	-141 ± 2	-200.8 ± 0.2
0.875	-274 ± 10	$1259. \pm 14.$	-2705 ± 7	114 ± 3	-169 ± 2	-175.5 ± 0.2
0.925	-323 ± 9	$1311. \pm 11.$	-2783 ± 6	113 ± 3	-198 ± 2	-152.3 ± 0.1
0.975	-405 ± 10	$1656. \pm 12.$	-3433 ± 7	127 ± 4	-244 ± 3	-136.4 ± 0.1

Table 5.6: C functions at different values of $\lvert\cos\theta_{\rm NR}\rvert$ from DEBRECEN. $C_z(y_{\rm cut})$ was found to be very small and therefore is not tabulated. The first column shows the center-of-bin value.

The simulation of massless four-parton configurations is also possible using the HERWIG 6.1 MC program. About 6 million events were produced, with about 2.5 million selected as four-jet events.

The ME option in PYTHIA, as was described for the four-jet rate in Section 5.3.1, is also tested for the corrections of the angular distributions.

Finally, a forth MC set was produced in order to check for mass effects. For this, the FOURJPHACT MC program is used [58], where the massive LO four-parton MEs are implied for generating the initial state. The showering and hadronization processes are modelled using PYTHIA 6.1 (standard parameters). The program allows to generate

$\cos\alpha_{34}$	$B_0(\mathrm{y_{cut}})$	$B_x(\mathrm{y_{cut}})$	$B_y(\mathrm{y_{cut}})$
-0.95	42.87 ± 0.04	-0.096 ± 0.006	3.559 ± 0.003
-0.85	38.83 ± 0.04	0.092 ± 0.006	3.680 ± 0.003
-0.75	36.79 ± 0.04	0.323 ± 0.006	3.872 ± 0.003
-0.65	34.62 ± 0.04	0.596 ± 0.006	4.072 ± 0.003
-0.55	33.00 ± 0.04	0.833 ± 0.006	4.292 ± 0.004
-0.45	31.21 ± 0.04	1.095 ± 0.005	4.526 ± 0.004
-0.35	29.93 ± 0.03	1.343 ± 0.005	4.797 ± 0.004
-0.25	28.51 ± 0.03	1.659 ± 0.005	5.074 ± 0.004
-0.15	27.62 ± 0.03	2.010 ± 0.005	5.395 ± 0.005
-0.05	26.76 ± 0.03	2.336 ± 0.005	5.781 ± 0.005
0.05	25.95 ± 0.03	2.754 ± 0.005	6.167 ± 0.006
0.15	25.18 ± 0.03	3.183 ± 0.006	6.575 ± 0.006
0.25	24.04 ± 0.03	3.640 ± 0.006	6.899 ± 0.006
0.35	22.88 ± 0.03	4.111 ± 0.007	7.171 ± 0.007
0.45	21.25 ± 0.02	4.425 ± 0.007	7.345 ± 0.007
0.55	19.43 ± 0.02	4.581 ± 0.008	7.235 ± 0.007
0.65	17.09 ± 0.02	4.393 ± 0.008	6.595 ± 0.007
0.75	13.81 ± 0.02	3.527 ± 0.007	4.978 ± 0.006
0.85	6.874 ± 0.01	1.275 ± 0.004	1.660 ± 0.003
0.95	0.338 ± 0.003	0.0186 ± 0.0003	0.0021 ± 0.0002

Table 5.7: B functions at different values of $\cos\alpha_{34}$ from DEBRECEN. The first column shows the center-of-bin value.

single final states only (such as $q\bar{q}gg$) or a correctly weighted mixture of final states.

5.3.2 Detector Corrections

The theoretical predictions, which are corrected to hadron level, have to be corrected further for detector effects such as acceptance, efficiency and resolution before being fitted to data. This is done by computing these observables from a MC before and after the detector simulation and imposing the same track and event selection cuts as for the data. Then the correction factors are computed,

$$C^{\mathrm{det}}(i_{bin}/\mathrm{y_{cut}}) = \frac{O_4^{\mathrm{det}}(i_{bin}/\mathrm{y_{cut}})}{O_4^{\mathrm{had}}(i_{bin}/\mathrm{y_{cut}})} \quad , \tag{5.8}$$

$\cos\alpha_{34}$	$C_0(\mathrm{y_{cut}})$	$C_x(\mathrm{y_{cut}})$	$C_y(\mathrm{y_{cut}})$	$C_{xx}(\mathrm{y_{cut}})$	$C_{xy}(\mathrm{y_{cut}})$	$C_{yy}(\mathrm{y_{cut}})$
-0.95	-208 ± 5	917 ± 7	-1899 ± 4	-26 ± 2	81.8 ± 0.8	-105.6 ± 0.1
-0.85	-182 ± 6	817 ± 8	-1718 ± 4	-11 ± 3	71 ± 1	-110.4 ± 0.1
-0.75	-185 ± 5	788 ± 6	-1615 ± 4	-12 ± 2	63 ± 1	-117.4 ± 0.1
-0.65	-160 ± 6	723 ± 7	-1521 ± 4	-1 ± 1	56 ± 1	-124.8 ± 0.1
-0.55	-146 ± 4	672 ± 6	-1435 ± 4	9 ± 2	49 ± 1	-132.2 ± 0.1
-0.45	-141 ± 4	641 ± 7	-1366 ± 4	11 ± 2	44 ± 2	-140.6 ± 0.1
-0.35	-141 ± 4	606 ± 6	-1300 ± 4	20 ± 2	36 ± 1	-149.5 ± 0.2
-0.25	-131 ± 4	572 ± 7	-1244 ± 4	28 ± 2	29 ± 1	-159.6 ± 0.2
-0.15	-123 ± 3	542 ± 7	-1200 ± 4	33 ± 3	19 ± 1	-171.9 ± 0.2
-0.05	-123 ± 3	529 ± 5	-1179 ± 4	43 ± 2	12 ± 1	-187.0 ± 0.2
0.05	-117 ± 4	512 ± 6	-1149 ± 4	51 ± 3	-2 ± 1	-201.5 ± 0.2
0.15	-111 ± 4	489 ± 7	-1107 ± 4	66 ± 3	-18 ± 1	-217.1 ± 0.2
0.25	-102 ± 3	455 ± 5	-1055 ± 4	76 ± 2	-30 ± 2	-231.4 ± 0.3
0.35	-98 ± 3	418 ± 5	-999 ± 4	82 ± 2	-43 ± 2	-243.5 ± 0.3
0.45	-83 ± 2	381 ± 4	-936 ± 3	95 ± 1	-60 ± 2	-253.8 ± 0.3
0.55	-72 ± 2	343 ± 4	-851 ± 3	100 ± 1	-72 ± 2	-253.6 ± 0.3
0.65	-70 ± 2	306 ± 4	-761 ± 3	95 ± 3	-78 ± 1	-238.3 ± 0.3
0.75	-48 ± 2	243 ± 4	-610 ± 3	76 ± 2	-69 ± 2	-183.7 ± 0.3
0.85	-24 ± 2	129 ± 2	-304 ± 1	23.4 ± 0.8	-29.9 ± 0.7	-63.6 ± 0.1
0.95	-1.3 ± 0.6	7.7 ± 0.8	-15.5 ± 0.3	0.4 ± 0.1	-0.54 ± 0.07	-0.86 ± 0.01

Table 5.8: C functions at different values of $\cos\alpha_{34}$ from DEBRECEN. $C_z(\mathrm{y_{cut}})$ was found to be very small and therefore is not tabulated. The first column shows the center-of-bin value.

where $O_4^{\mathrm{det}}(i_{bin}/\mathrm{y_{cut}})$ denotes the value of the observable at the detector level. The hadron level distributions are obtained by switching off any photon radiation in the initial and final state (ISR, FSR), both present at the detector level, with all particles having mean lifetimes less than 10^{-9} s required to decay, and all other particles being treated as stable. The detector level distributions come from the full MC simulation described in Section 5.1. Starting from the distributions at HL, $O_4^{\mathrm{corrHL}}(i_{bin}/\mathrm{y_{cut}})$, the detector-corrected distribution, $O_4^{\mathrm{corrDL}}(i_{bin}/\mathrm{y_{cut}})$, is obtained according to

$$O_4^{\mathrm{corrDL}}(i_{bin}/\mathrm{y_{cut}}) = C^{\mathrm{det}}(i_{bin}/\mathrm{y_{cut}}) O_4^{\mathrm{corrHL}}(i_{bin}/\mathrm{y_{cut}}) \quad . \tag{5.9}$$

The detector correction factors are typically found within the 5% range, except at the edges of the phase space where corrections up to 10-20% are observed.

$\ln(y_{cut})$	$B_0(y_{cut})$	$B_x(y_{cut})$	$B_y(y_{cut})$
-2.2	0.00939 ± 0.00003	0.000888 ± 0.000005	0.002900 ± 0.000009
-2.4	0.06333 ± 0.00009	0.005412 ± 0.00002	0.01732 ± 0.00002
-2.6	0.2318 ± 0.0002	0.01959 ± 0.00004	0.05910 ± 0.00004
-2.8	0.6059 ± 0.0004	0.05025 ± 0.00008	0.14687 ± 0.00007
-3.0	1.2991 ± 0.0006	0.1068 ± 0.0001	0.3036 ± 0.0001
-3.2	2.4394 ± 0.0009	0.1981 ± 0.0002	0.5529 ± 0.0002
-3.4	4.166 ± 0.001	0.3380 ± 0.0003	0.9220 ± 0.0002
-3.6	6.650 ± 0.002	0.5418 ± 0.0004	1.4418 ± 0.0003
-3.8	10.067 ± 0.003	0.8205 ± 0.0006	2.1424 ± 0.0005
-4.0	14.612 ± 0.004	1.1964 ± 0.0008	3.0570 ± 0.0006
-4.2	20.538 ± 0.005	1.684 ± 0.001	4.2248 ± 0.0009
-4.4	28.059 ± 0.007	2.305 ± 0.001	5.687 ± 0.001
-4.6	37.406 ± 0.009	3.087 ± 0.002	7.471 ± 0.002
-4.8	48.89 ± 0.01	4.054 ± 0.003	9.630 ± 0.002
-5.0	62.80 ± 0.02	5.232 ± 0.003	12.215 ± 0.003
-5.2	79.46 ± 0.02	6.636 ± 0.004	15.277 ± 0.004
-5.4	99.26 ± 0.03	8.319 ± 0.005	18.831 ± 0.005
-5.6	122.39 ± 0.04	10.319 ± 0.007	22.923 ± 0.006
-5.8	149.56 ± 0.05	12.642 ± 0.009	27.634 ± 0.008
-6.0	180.99 ± 0.07	15.34 ± 0.01	33.05 ± 0.01
-6.2	217.14 ± 0.09	18.48 ± 0.02	39.12 ± 0.01
-6.4	258.4 ± 0.1	22.16 ± 0.02	46.02 ± 0.02
-6.6	304.8 ± 0.1	26.32 ± 0.02	53.71 ± 0.02
-6.8	357.7 ± 0.2	31.09 ± 0.03	62.33 ± 0.03
-7.0	416.2 ± 0.2	36.47 ± 0.04	71.71 ± 0.04
-7.2	481.5 ± 0.3	42.35 ± 0.05	82.08 ± 0.05
-7.4	555.0 ± 0.4	48.92 ± 0.06	93.69 ± 0.06
-7.6	636.4 ± 0.5	56.43 ± 0.08	106.03 ± 0.07
-7.8	727.9 ± 0.6	65.2 ± 0.1	119.71 ± 0.09
-8.0	828.3 ± 0.8	74.3 ± 0.1	134.4 ± 0.1

Table 5.9: B functions for the four-jet rate from DEBRECEN at different values of y_{cut}. Bins from -0.2 to -1.8 are not tabulated because no event was found to be a four-jet event for those values of y_{cut}. The values for bins with $\ln(y_{cut})$ smaller than -8 are not in the table as we are not interested in the four-jet rate at too small y_{cut} values.

$\ln(y_{cut})$	$C_0(y_{cut})$	$C_x(y_{cut})$	$C_y(y_{cut})$	$C_{xx}(y_{cut})$	$C_{xy}(y_{cut})$	$C_{yy}(y_{cut})$
-2.2	0.032 ± 0.004	0.148 ± 0.005	-0.318 ± 0.005	0.014 ± 0.001	0.019 ± 0.002	-0.0678 ± 0.0002
-2.4	0.201 ± 0.009	1.01 ± 0.01	-2.20 ± 0.01	0.093 ± 0.003	0.106 ± 0.003	-0.4153 ± 0.0006
-2.6	0.64 ± 0.02	3.80 ± 0.02	-8.20 ± 0.02	0.334 ± 0.007	0.338 ± 0.006	-1.441 ± 0.001
-2.8	1.64 ± 0.03	10.13 ± 0.04	-21.74 ± 0.03	0.84 ± 0.01	0.76 ± 0.01	-3.677 ± 0.002
-3.0	3.18 ± 0.06	22.1 ± 0.1	-47.25 ± 0.05	1.83 ± 0.03	1.43 ± 0.02	-7.780 ± 0.003
-3.2	4.77 ± 0.07	42.09 ± 0.09	-90.01 ± 0.08	3.40 ± 0.03	2.37 ± 0.03	-14.547 ± 0.005
-3.4	6.1 ± 0.1	73.6 ± 0.2	-156.3 ± 0.1	5.82 ± 0.04	3.56 ± 0.04	-24.944 ± 0.008
-3.6	6.4 ± 0.2	119.4 ± 0.3	-254.1 ± 0.2	9.41 ± 0.07	4.86 ± 0.06	-40.07 ± 0.01
-3.8	3.3 ± 0.3	184.6 ± 0.3	-392.5 ± 0.3	14.40 ± 0.08	6.42 ± 0.08	-61.23 ± 0.02
-4.0	-6.1 ± 0.4	272.8 ± 0.4	-582.4 ± 0.4	21.1 ± 0.1	7.8 ± 0.1	-89.87 ± 0.02
-4.2	-25.3 ± 0.5	390.2 ± 0.8	-835.9 ± 0.5	29.9 ± 0.2	9.0 ± 0.2	-127.77 ± 0.03
-4.4	-61.3 ± 0.6	541.7 ± 0.9	-1167.4 ± 0.7	41.3 ± 0.3	9.1 ± 0.2	-176.72 ± 0.04
-4.6	-118.7 ± 0.9	732 ± 1	-1596.0 ± 0.8	54.9 ± 0.3	8.8 ± 0.3	-238.85 ± 0.06
-4.8	-209 ± 1	971 ± 1	-2139 ± 1	72.6 ± 0.4	6.5 ± 0.4	-316.24 ± 0.08
-5.0	-346 ± 1	1267 ± 2	-2818 ± 2	94.1 ± 0.6	1.3 ± 0.6	-412.0 ± 0.1
-5.2	-536 ± 2	1616 ± 3	-3657 ± 2	122.2 ± 0.9	-5.9 ± 0.7	-528.6 ± 0.2
-5.4	-807 ± 3	2042 ± 9	-4683 ± 3	$154 \pm 2.$	-18.0 ± 0.9	-668.5 ± 0.2
-5.6	-1173 ± 4	2555 ± 4	-5932 ± 4	188 ± 1	-33 ± 1	-835.5 ± 0.3
-5.8	$-1664 \pm 5.$	3145 ± 6	-7431 ± 4	230 ± 2	-56 ± 1	-1033.1 ± 0.4
-6.0	-2302 ± 6	3837 ± 7	-9221 ± 6	282 ± 2	-89 ± 2	-1264.1 ± 0.5
-6.2	-3135 ± 9	4634 ± 11	-11324 ± 8	339 ± 3	-135 ± 3	-1533.2 ± 0.7
-6.4	-4205 ± 11	5569 ± 13	-13810 ± 10	401 ± 4	-188 ± 3	-1841.7 ± 0.9
-6.6	-5551 ± 17	6615 ± 18	-16732 ± 13	469 ± 4	-250 ± 4	-2199 ± 1
-6.8	-7178 ± 18	7780 ± 26	-20132 ± 17	520 ± 4	-342 ± 5	-2608 ± 2
-7.0	-9259 ± 22	9102 ± 32	-24009 ± 24	666 ± 9	-449 ± 7	-3068 ± 2
-7.2	-11510 ± 145	10501 ± 103	-28562 ± 31	798 ± 21	-578 ± 10	-3590 ± 3
-7.4	-14797 ± 40	12188 ± 79	-33681 ± 37	907 ± 30	-732 ± 11	-4184 ± 3
-7.6	-18454 ± 56	14087 ± 59	-39542 ± 49	1016 ± 15	-923 ± 14	-4847 ± 4
-7.8	-22856 ± 64	16098 ± 81	-46281 ± 63	1158 ± 19	-1139 ± 18	-5584 ± 5
-8.0	-28024 ± 102	18350 ± 116	-53836 ± 78	1275 ± 25	-1416 ± 22	-6384 ± 7

Table 5.10: C functions for the four-jet rate from DEBRECEN at different values of y_{cut}. Bins from -0.2 to -1.8 are not tabulated because no event was found to be a four-jet event for those values of y_{cut}. The values for bins with $\ln(y_{cut})$ smaller than -8 are not in the table as we are not interested in the four-jet rate at too small y_{cut} values.

Another approach is tested for the correction of the angular correlations. A detector level distribution is obtained by passing through the detector simulation events simulated with the PYTHIA four-parton option, including ISR and FSR. This MC simulation was expected to describe the data better. This was indeed found for $\cos\alpha_{34}$, but surprisingly not for $\cos\theta_{NR}$ as shown in Fig. 5.1. This may be a hint of some problems in the tuning or in the showering and hadronization processes implemented in PYTHIA. In this analysis,

this new MC simulation has been used to calculate again $C^{\rm det}$ factors, but only for $\cos\alpha_{34}$, were an improvement has been observed.

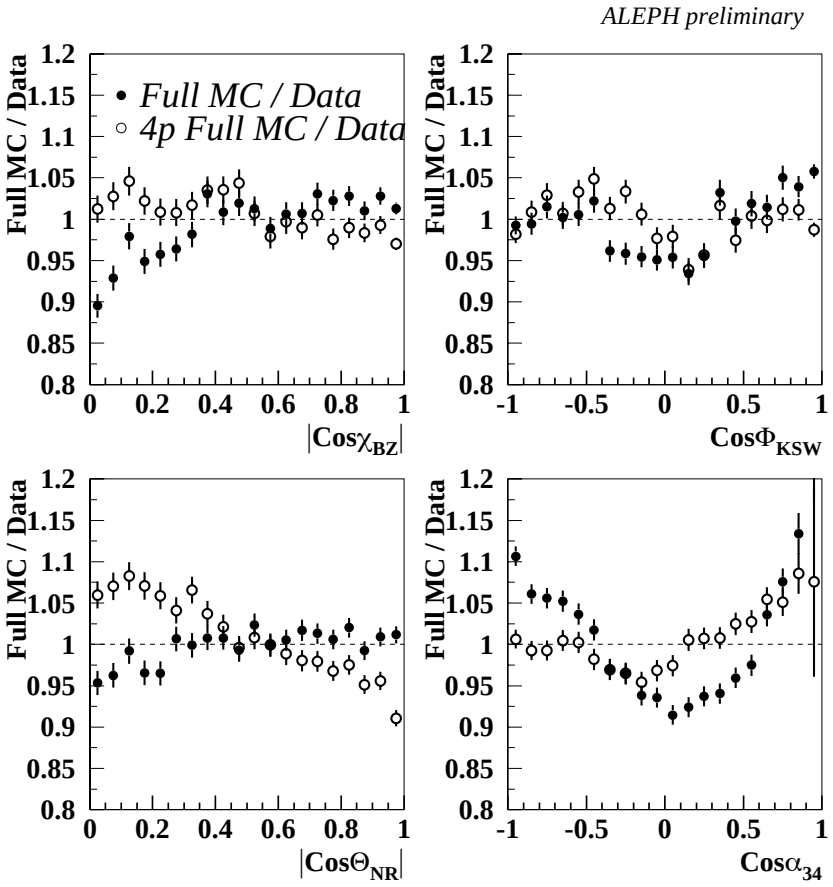

Figure 5.1: Comparison of the two sets of full MC simulations with respect to ALEPH data.

5.4 The fit procedure

The measured distributions for the four-jet angular correlations and the four-jet rate are put together to form a vector

$$D_{1\ldots140} = (\cos\chi_{\mathrm{BZ}\,1\ldots20}, \cos\phi_{\mathrm{KSW}\,1\ldots20}, \cos\theta_{\mathrm{NR}\,1\ldots20}, \cos\alpha_{34\,1\ldots20}, R_{4\,1\ldots60}). \tag{5.10}$$

A covariance matrix σ^D_{ij} is calculated from data distributions to take into account the statistical error, correlations between bins of a single distribution, and correlations between

bins of different distributions. The diagonal block elements are the covariance matrices of the single distributions. For the four-jet angular correlations they are multinomial, i.e.

$$\begin{aligned}(\sigma_{ij}^D)_{i,j\in\text{same angle}} &= -p_i p_j \frac{1}{N_{\text{had}}} \\ (\sigma_{ii}^D) &= p_i \left(\frac{1}{\Delta} - p_i\right) \frac{1}{N_{\text{had}}}\end{aligned} \tag{5.11}$$

where $p_i = N_i/N_{\text{had}}\Delta$ with N_i the number of entries in a single bin, N_{had} the total number of hadronic events and Δ the bin width. For the four-jet rate, being a different observable at each y_{cut} value, the formulas to be used are the ones of the off-diagonal block elements,

$$(\sigma_{ij}^D)_{i,j\in\text{diff. dist.}} = ((pp)_{ij} - p_i p_j)\,\frac{1}{N_{\text{had}}} \tag{5.12}$$

where $(pp)_{ij} = N_{ij}/\left(N_{\text{had}}\Delta^2\right)$ with N_{ij} the number of events common to bin i of one distribution and bin j of another.

Then a further vector is formed, $T_{1\ldots140}$, with the theoretical distributions corrected to detector level, having the same dimension as the data vector. With all these inputs, the following function is computed and minimized with respect to the fitted parameters:

$$\chi^2 = \sum_{i,j\in\text{fit range}} \delta_i \sigma_{ij}^{-1} \delta_j \quad , \quad \delta_i = D_i - T_i \quad , \quad \sigma_{ij} = \sigma_{ij}^D + \sigma_{ij}^T. \tag{5.13}$$

5.5 Systematic Uncertainty Studies

Systematic uncertainties can arise from imperfections of the implementation of the physics processes in the MC as well as from deficiencies in the description of the detector performance, from theoretical uncertainties or missing higher orders in the perturbative series, from the model used to calculate the hadronization corrections, and from the specific analysis procedure. The sources of systematic uncertainty that have been taken into account are: the fit range, the selection cuts, the hadronization and background corrections, the detector corrections, the scale uncertainty and the mass effects in the four-jet angular correlations.

In general a Bayesian method is used [21, 44] in order to obtain the systematic error for each source, except for the variation of the fit range, where the number of fitted bins is different. This scheme tries to reduce the arbitrariness of the estimation of the total systematic error: how many and which variations have to be applied in the analyses and the weight that each source should have in the calculation of the final systematic error.

The main decision criterion for the weight in this thesis is the quality of the fit when using a particular analysis chain, i.e. the overall χ^2. The Bayesian idea is that *a priori* all models can be considered equally well suited for usage in the analysis, but from a bad χ^2 it is deduced that the *a posteriori* probability of such model is low, and therefore this model should get a small weight when estimating the actual systematic error. From classical statistics it is known that in the large sample limit a deviation from the estimator of a parameter by N times its variance corresponds to an increase in χ^2 of N^2. This will be the basis for the definition of the size of the systematic error.

For example, a measurement of two quantities (x, y) results in a set of numbers (x_0, y_0, χ_0^2), (x_1, y_1, χ_1^2), ..., (x_n, y_n, χ_n^2) after $(n+1)$ variations of the analysis procedure, with $\chi_0^2 = \min_{i=0,n}\chi_i^2$. First a correlation coefficient for the systematic errors is calculated according to

$$\rho_{x,y}^{\text{syst}} = \frac{\sum_{i=1}^{n}(x_0 - x_i)(y_0 - y_i)}{\sqrt{\left(\sum_{i=1}^{n}(x_0 - x_i)^2\right)\left(\sum_{i=1}^{n}(y_0 - y_i)^2\right)}} \quad . \tag{5.14}$$

Then the elements of the systematic covariance matrix are defined as

$$\sqrt{\sigma_{x,x}^{\text{syst}}} = C \max_{i=1,n}\left(\frac{\Delta x_i}{\sqrt{\Delta\chi^2}}\right) \quad , \quad \sigma_{x,y}^{\text{syst}} = \rho_{x,y}^{\text{syst}}\sqrt{\sigma_{x,x}^{\text{syst}}}\sqrt{\sigma_{y,y}^{\text{syst}}} \, , \tag{5.15}$$

with

$$\Delta x_i = |x_0 - x_i| \quad , \quad \Delta\chi^2 = \max(1, |\chi_0^2 - \chi_i^2|) \quad , \quad C = \max\left(1, \sqrt{\chi_0^2/N_{\text{dof}}}\right) . \tag{5.16}$$

The factor C takes into account cases where the best fit gives a bad χ^2. This scheme is generalizable to any number of fit variables, and it is ensured that models giving a bad fit are properly deweighted. Of course still some unavoidable arbitrariness remains in the choice and number of variations.

$\ln(y_{cut})$	$B_4(y_{cut})$	$C_4(y_{cut})$
-2.0	0.000502 ± 0.000007	0.0136 ± 0.004
-2.2	0.01247 ± 0.00004	0.33 ± 0.01
-2.4	0.0820 ± 0.0001	2.15 ± 0.02
-2.6	0.2981 ± 0.0002	7.89 ± 0.05
-2.8	0.7741 ± 0.0004	20.64 ± 0.08
-3.0	1.6532 ± 0.0006	44.6 ± 0.3
-3.2	3.0924 ± 0.0009	83.0 ± 0.2
-3.4	5.272 ± 0.001	142.1 ± 0.4
-3.6	8.409 ± 0.002	226.1 ± 0.5
-3.8	12.717 ± 0.003	341.3 ± 0.6
-4.0	18.450 ± 0.004	490 ± 1
-4.2	25.911 ± 0.006	680 ± 2
-4.4	35.377 ± 0.007	910 ± 2
-4.6	47.15 ± 0.01	1181 ± 3
-4.8	61.62 ± 0.01	1503 ± 3
-5.0	79.15 ± 0.02	1870 ± 5
-5.2	100.13 ± 0.02	2270 ± 5
-5.4	125.04 ± 0.03	2700 ± 10
-5.6	154.20 ± 0.04	3161 ± 9
-5.8	188.37 ± 0.05	3596 ± 15
-6.0	227.90 ± 0.07	4049 ± 16
-6.2	273.39 ± 0.09	4435 ± 22
-6.4	325.5 ± 0.1	4763 ± 24
-6.6	384.1 ± 0.2	4915 ± 36
-6.8	451.1 ± 0.2	4757 ± 243
-7.0	525.1 ± 0.2	4784 ± 58
-7.2	607.5 ± 0.3	4456 ± 86
-7.4	700.2 ± 0.4	3384 ± 100
-7.6	803.1 ± 0.5	2097 ± 107
-7.8	919.4 ± 0.6	128 ± 152
-8.0	1045.9 ± 0.8	-2562 ± 246

Table 5.11: B and C functions for the four-jet rate from DEBRECEN at different values of y_{cut}. Here the contributions from different columns in tables 5.9 and 5.10 have been added taking the $SU(3)$ values for the colour factor ratios. Bins from -0.2 to -1.8 are not in the table because no event was found to be a four-jet event for those values of y_{cut}. The values for bins with $\ln(y_{cut})$ smaller than -8 are not in the table as we are not interested in the four-jet rate at too small y_{cut} values.